Electronic Supplementary Information for

Selective CO_2 Electroreduction to Multicarbon Products Exceeding 2 A cm^{-2} in Strong Acid via a Hollow-Fiber Cu Penetration Electrode†

Chang Zhu,‡[abc] Gangfeng Wu,‡[ab] Aohui Chen,[ad] Guanghui Feng,[abc] Xiao Dong,[a] Guihua Li,[ab] Shoujie Li,[a] Yanfang Song,[a] Wei Wei,*[abd] Wei Chen,*[ab]

[a] CAS Key Laboratory of Low-Carbon Conversion Science and Engineering Center, Shanghai Advanced Research Institute, Chinese Academy of Sciences, Shanghai 201210, P.R. China
[b] University of Chinese Academy of Sciences, Beijing, 100049, P.R. China.
[c] Key Laboratory of Biomass Chemical Engineering of Ministry of Education College of Chemical and Biological Engineering, Zhejiang University, Hangzhou 310027, P.R. China.
[d] School of Physical Science and Technology, ShanghaiTech University, Shanghai 201210, P.R. China
‡ These authors contributed equally to this work
* E-mail: chenw@sari.ac.cn, weiwei@sari.ac.cn

Materials and methods

Chemicals and Materials

Cu powder (99% purity, 1 μm) was purchased from Shanghai Xiangtian Nano Materials Co., Ltd, Polyether sulfone resin (PES) from Saudi Basic Industries Corporation (SABIC). Nafion 117 membrane was purchased from DuPont. N-methyl-2-pyrrolidone (NMP), sodium borohydride ($NaBH_4$), Sulfuric acid (H_2SO_4), and potassium chloride (KCl) were purchased from Sinopharm Chemical Reagent Co., Ltd. 3-Trimethylsilyl-1-propane sulfonic acid sodium salt (DSS) was purchased from Tokyo Chemical Industry Co., Ltd, Deuterium oxide (D_2O) was purchased from Sigma-Aldrich. All chemicals were used as received without further purification. Electrolyte solutions were prepared using 18.2 MΩ H_2O (Master-S30UVF water purification system).

Preparation of Cu hollow fiber penetration electrode

Cu hollow fiber was prepared by a phase-inversion/sintering process.[1] Briefly, commercially available Cu powder (99%, 1 μm) was used as an inorganic phase in the preparation of catalysts, N-methyl pyrrolidone (NMP, 99.5%) and polyethersulfone resin (PES, Ultem 1000) were used as solvents and polymers, respectively. Cu powder (60 wt%) was first added to NMP (30 wt%) for ultrasonic treatment for 30 min and then PES (10 wt%) was added to the mixture for stirring to mix it. The as-obtained mixture was further treated by ball-milling (300 rpm) for 10 h to form a uniform slurry. After cooling down to room temperature, the slurry was vacuumed for 4 h to remove the bubbles and then obtain a casting liquid. Next, the casting liquid was extruded through the spinning machine and shaped in the tap water bath via the phase-inversion process. Directly after spinning the as-formed tubes were kept in a water bath

for 24 h for completion of the solvent elimination, followed by drying and stretching for 48 h to obtain the green body. The green body was firstly cut into appropriate lengths and sintered in an air atmosphere at 600 ^{o}C (heating rates: 5 ^{o}C min^{-1}) for 4 h to remove PES. The oxidized fiber was first reduced with 0.2 M $NaBH_4$ solution, and then further reduced and sintered in the gas flow of 5% H_2 in balance gas Argon at 500 ^{o}C (heating rate: 5 ^{o}C min^{-1}) for 3 h to obtain Cu hollow fiber. As-synthesized Cu hollow fiber was stored in the Ar atmosphere to prevent oxidation for standby.

Each Cu hollow fiber was stuck into a copper tube using conductive silver adhesive for electrical contact, while the ends of the Cu hollow fiber, as well as the joints between the Cu hollow fiber and copper tube, were sealed and covered with gas-tight and nonconductive epoxy. After drying at room temperature for 12 h, a working Cu hollow fiber penetration electrode (Cu HPE) was obtained, and the exposed length of the Cu HPE was 2 cm. For the Cu HPE array, the exposure length of the single Cu HPE tube was 2.2 cm and the geometric area was 5.2 cm^2 ($S = n\pi D_{out}L$ = 10×3.14×750×0.0001×2.2 = 5.2 cm^2, where S is the electrode area, n is the number of hollow fiber tubes, D_{out} is the outer diameter of the hollow fiber, and L is the length of the hollow fiber).

Characterizations

The cross-section and surface morphology of hollow fiber was observed by a SUPRRATM 55 SEM with an accelerating voltage of 5.0 kV. Powder XRD was analyzed in the 2θ range 5° to 90° using a Rigatku Ultima 4 x-ray diffractometer with Cu Ka radiation, operating at 40 kV and 40 mA and in the step mode (0.0167°). X-ray photoelectron spectroscopy (XPS) was conducted using a Quantum 2000 Scanning ESCA Microprobe instrument with a

monochromatic Al Kα source (1486.6 eV). The peaks of Cu XPS and Cu auger were recorded in the binding energy ranges of 925-965 eV and 555-585 eV, respectively. The binding energies in all XPS spectra were calibrated according to the C 1s peak (284.8 eV). The nanostructure of catalysts was investigated by an ac-STEM instrument (JEM-ARM300F) at 300 kV and a FEI Tecnai G2 F20 S-Twin HRTEM, which was operated at 200 kV.

Electrochemical measurements

The acidic CO_2ERR performance was evaluated at ambient temperature and pressure on the Biologic VMP3 potentiostat using the gas-tight electrolysis cell, which comprised two same compartments made of quartz glass with the inner height of 5.0 cm, the inner length of 5.0 cm, and the inner side of 1.5 cm. The high-purity and transparent quartz H-cell including two parts of cathodic compartment and anodic compartment (5.0 cm*5.0 cm*1.5 cm) is conducive to heat dissipation and in-situ characterization during the electrolysis process. As shown in Fig. S6, the cathodic and anodic compartments were separated by a Nafion 117 membrane. A KCl-saturated Ag/AgCl electrode and a Pt net were used as the reference and counter electrode, respectively. H_2SO_4 containing various contents of KCl or different pH was used as catholyte, and 0.05 M H_2SO_4 aqueous solution was used as anolyte. Both the anolyte and catholyte solutions were cycled and refreshed in anodic and cathodic compartments with a fixed flow rate of 20 mL min^{-1} by using two identical peristaltic pumps (JIHPUMP BT-50EA 153YX). And both catholyte and anolyte storage tanks had the same volume of 20 L, which were placed in a constant-temperature (25.0 ℃) water bath to maintain the electrolyte temperature constant. And the solutions were also accompanied by the

supplement of ultrapure water to maintain a constant concentration of electrolyte. The exhaust from the cathodic compartment was measured by the on-line GC during the whole test. The concentration of liquid reduction products in the circulating cathodic electrolyte can be analyzed by off-line GC.

A Biologic VMP3 potentiostat was used for potential/current control and measurement. Under situations with a very large current (>400 mA), the Biologic VMP3 potentiostat was connected to a VMP3 booster chassis with a 10 A current option. All the potentials were recorded against an Ag/AgCl (saturated KCl) reference electrode and then converted to those versus reversible hydrogen electrode (RHE) using the equation:

$$E\ (vs.\ RHE) = E(vs.\ Ag/AgCl) + 0.197\ V + 0.0591\ V \times pH + iR_s$$

where *E (vs. Ag/AgCl)* is the applied potential, *pH* is the *pondus hydrogenii* value of the electrolyte solutions (Table S8), *i* is the current density at each applied potential, and R_s is the solution resistance obtained by EIS measurements (Table S9).

For the long-term performance test of CO_2 electroreduction, the current density fixed at -2 A cm^{-2} was applied on the Cu HPE. The electrolyte was sulfuric solution with 3 M KCl (pH = 0.71), and the CO_2 flow rate remained at 20 mL min^{-1}. The catholyte and anolyte were cycled with the flow rate of 20 mL min^{-1}. The exhaust from the cathodic compartment was measured by the on-line GC during the whole 100-hour test.

Galvanostatic electrochemical impedance spectroscopy (EIS) was performed at each fixed current following each galvanostatic CO_2 electrolysis. The frequency limits were typically set in the range from 100k Hz to 10 Hz with a perturbation amplitude of 10% of the base current. The electrochemically active surface area (ECSA) of the electrode was evaluated by the double layer

capacitance (C_{dl}). The C_{dl} was determined by performing cyclic voltammetry (CV) at the potential range of -0.45 to -0.4 V (vs. Ag/Ag^{+}) at different scan rates. The slop of the plot current density against the scan rate gave the value of C_{dl}.

All potentials applied in the main text and Supplementary Materials were referred to RHE unless otherwise stated.

Product quantification

Gaseous products:

Gas products were analyzed by an on-line gas chromatography (GC), and liquid products were analyzed by offline GC and ^{1}H nuclear magnetic resonance (^{1}H-NMR) spectrometer. The exhaust from the cathodic compartment during the entire 100-hour test directly enter the gas chromatograph (GC-2014, Shimadzu) equipped with a Molecular sieve-13X 60/80 column and a Plot-Q80/100 column using flame ionization detector (FID) during the electrochemical reactions and analyzed online, the product H_2 from the cathode compartment was also analyzed using a thermal conductivity detector (TCD). A GC run was initiated every 15 min. The faradaic efficiency of a specific product is calculated as follows:

$$FE = \frac{C_{product} \times 10^{-6} \times v_{CO2} \times 10^{-3} \times t \times \alpha \times 96485}{22.4 \times Q} \times 100\%$$

where C_{product} is the concentration of the gas-phase products, v_{CO_2} is the flow rate of CO_2, α is the number of electrons transferred from CO_2 to products, t is the reaction time, Q (A·s) is the total quantity of electric charge.

Liquid products:

The mixed catholyte without separating the liquid products was sampled at a 5-hour interval for quantitative measurement through offline GC-2014 (Shimadzu) equipped with an autosampler and an OVI-G43 capillary column (Supelco, USA). Catholyte were further analysed by using a 600 MHz ^{1}H-NMR spectrometer (Bruker), with DSS and D_2O as internal standards. After electrochemical reduction, an electrolyte solution (0.5 mL) containing liquid products of electrical reduction was mixed with 0.1 mL 3-Trimethylsilyl-1-propane sulfonic acid sodium salt (DSS, Tokyo Chemical Industry Co.) (6 mM) and 0.1 mL deuterium oxide (D_2O, Sigma-Aldrich) for use as internal standards. The faradaic efficiency (%) and yields (mmol cm^{-2} h^{-1}) of liquid products were calculated as follows:

$$FE = \frac{C_{product} \times 10^{-6} \times V \times \alpha \times 96485}{M_{product} \times Q} \times 100\%$$

where $C_{product}$ (mg·L^{-1}) is the concentration of liquid products, V (mL) is the liquid volume in the cathode chamber, α is the number of electrons transferred from CO_2 to products, $M_{product}$ (g·mol^{-1}) is the molecular weight of products, Q (A·s) is the total quantity of electric charge.

The SPCE of CO_2 towards producing C_{2+} was calculated as follows at 25 °C, 1 atm:

$$SPCE = \frac{(j \times 60s)/(N \times F)}{(v \times 1(min))/V_m}$$

where j means the partial current density of C_{2+}, N stands for electron transfer.

By assuming that the overpotential of oxygen evolution reaction on the anode side is zero, the cathodic energy efficiency (EE_i, %) for reduction product was calculated as follows:

$$EE_i = \frac{1.23 - E_i}{1.23 - E} \times FE_i \times 100\%$$

Where E is the applied potential vs RHE, E_i is the thermodynamic potential for obtaining corresponding reduction product i, which is 0.08, 0.09, and 0.10 V (vs. RHE) for C_2H_4, EtOH, and PrOH from CO_2ERR, respectively. The thermodynamic potential for water oxidation in the anode side is 1.23 V vs. RHE.

In situ measurements

In situ ATR-FTIR measurements were performed on Nicolet iS50 equipped with liquid nitrogen-cooled MCT detector. A silicon semi cylindrical prism is used as the conductive base of catalyst and infrared reflector. The catalyst was suspended on the Au/Si surface as a working electrode. The mass load of catalyst was 1 mg cm^{-2}, the electrolyte was 0.005 M H_2SO_4 with 0.1 M K_2SO_4, and CO_2 was constantly used for purification during the experiment. All ATR-FTIR measurements were acquired by averaging 32 scans at a spectral resolution of 4 cm^{-1}. For CO_2ERR, chronoamperometric tests were conducted from 0 to −1.1 V vs. RHE stepwise. The spectra under open circuit potential (OCP) were recorded as comparison.

The concentration of H^+ in the electrolyte solution was measured by acid-base titration, 0.1 M NaOH (20 mL) was used as the standard solution for acid quantification, and phenolphthalein as the indicator, to record the electrolyte volume consumed when the NaOH solution changes from red to transparent, and then the concentration of H^+ in the electrolyte solution was calculated.

COMSOL multiphysics simulations

The spatial distribution of near

surface pH values of catalytic electrodes under different operating currents was calculated using the Tertiary Current Distribution module in a simplified one-dimensional model using finite element simulation (Table S10). Specifically, one end of the one-dimensional simulation area is set as the working electrode surface, and the other side is set as the bulk concentration to describe the bulk electrolyte. The electrode surface undergoes a reduction reaction, its current characteristics follow the Bulter Volmer equation and the Nernst equation, its potential characteristics follow the Nernst equation, the concentration of the opposite body phase is set to the corresponding initial concentration, and the ion migration in the simulation area follows the Nernst Planck equation. The solution process is based on the MUMPS (multiple massively parallel spark direct solver) steady-state solver, and the relative tolerance and residual factor are set to 1E-8 and 1, respectively, eight layers of boundary layer subdivision are set on the simulated electrode surface to ensure the accuracy of the simulation results. The pH distribution near the electrode surface was calculated by solving the operating current from 0-3000mA cm^{-2} at bulk pH of 0, 1, 2, and 3, respectively.

The electrode surface reaction follows the BV equation:

$$i_{loc} = i_0(\exp\left(\frac{\alpha_a F\eta}{RT}\right) - exp(\frac{-\alpha_c F\eta}{RT}))$$

The balance potential follows the Nernst equation:

$$E_{eq} = -\frac{\Delta G}{nF}$$

The transfer of dilute substances follows Fick law:

$$N_i = J_i = -D_i \nabla c_i$$

$$\frac{\partial c_i}{\partial t} + \nabla \cdot N_i = R_{i,tot}$$

The transportation of electricity follows the Nernst Planck relationship:

$$N_i = -D_i \nabla c_i - z_i u_{m,i} F c_i \nabla \emptyset_l + u c_i = J_i + u c_i$$

$$E_{eq} = E_{eq,ref} - \frac{RT}{nF} ln \prod_i \left(\frac{a_i}{a_{i,ref}}\right)^{\nu_i}$$

DFT calculations

All the calculations are performed in the framework of the density functional theory with the projector augmented plane-wave method, as implemented in the Vienna ab initio simulation package.[2] The generalized gradient approximation adopted with the Perdew, Burke, and Ernzerhof is selected for the exchange-correlation potential.[3] Our calculations have used a slab model composed of four layers of 4 × 3 × 3 representing the Cu (111) surfaces separated by 15 Å of vacuum space. The cut-off energy for plane wave is set to 520 eV. The energy criterion is set to 10^{-5} eV in iterative solution of the Kohn-Sham equation. The Brillouin zone was sampled with allowed spacing between k points in 0.2 $Å^{-1}$, with Γ-centered Monkhorst−Pack k-point grid. For the constructed slab model calculations, the vacuum distance was carefully tested and set to be 12 Å to avoid the cell-to-cell interactions. The 3 × 3 × 1 Monkhorst k-point meshes were used for the Brillouin-zone integrations of supercell models. All the structures are relaxed until the residual forces on the atoms have declined to less than 0.01 eV/Å. The 3D charge density plot is employed by VESTA software.[4]

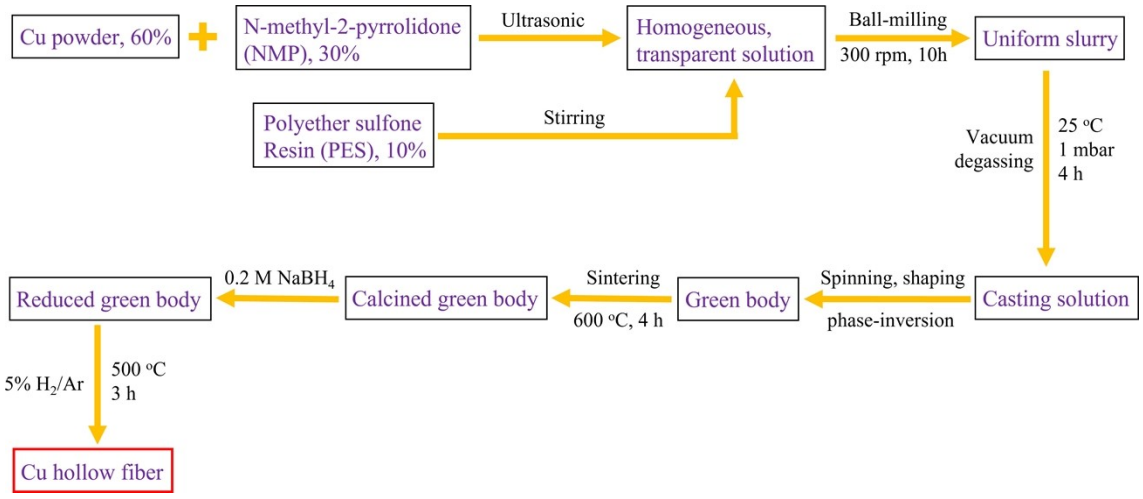

Fig. S1. Schematic illustration showing the general procedures for the fabrication of Cu hollow fiber.

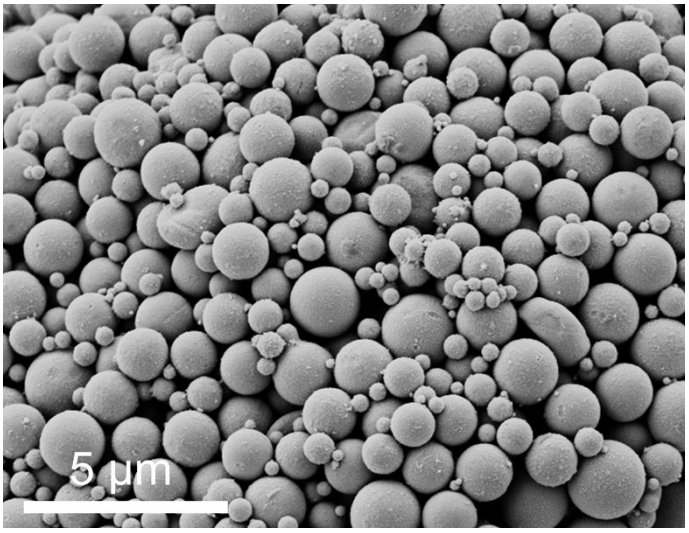

Fig. S2. SEM image of commercially available copper powder.

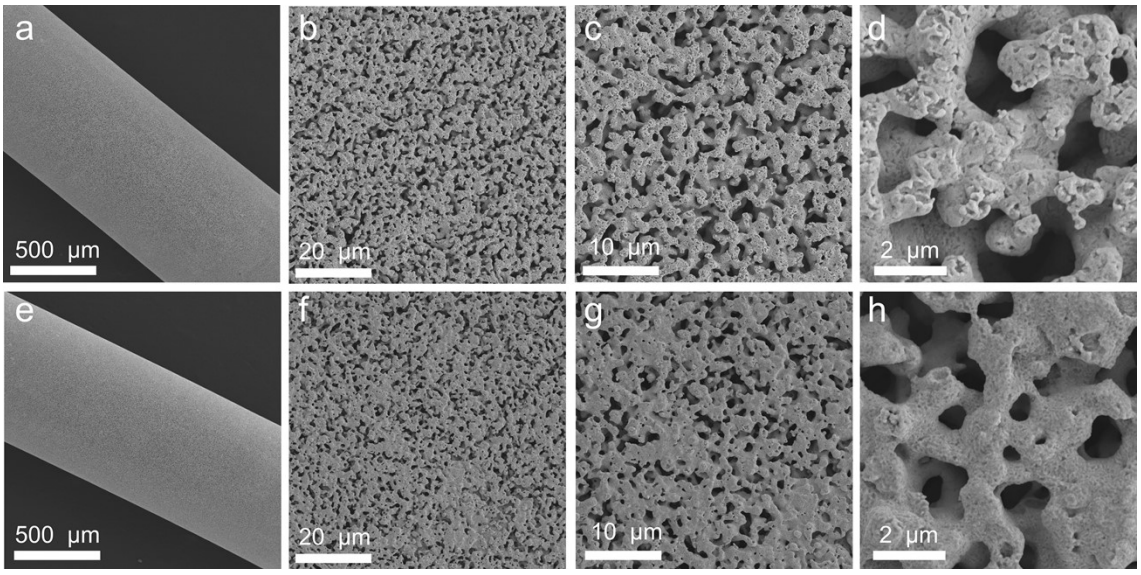

Fig. S3. SEM images of the outer surface of (a-d) pre-reaction Cu HPE and (e-h) post-reaction Cu HPE-100 h with low, medium, and high magnifications, respectively.

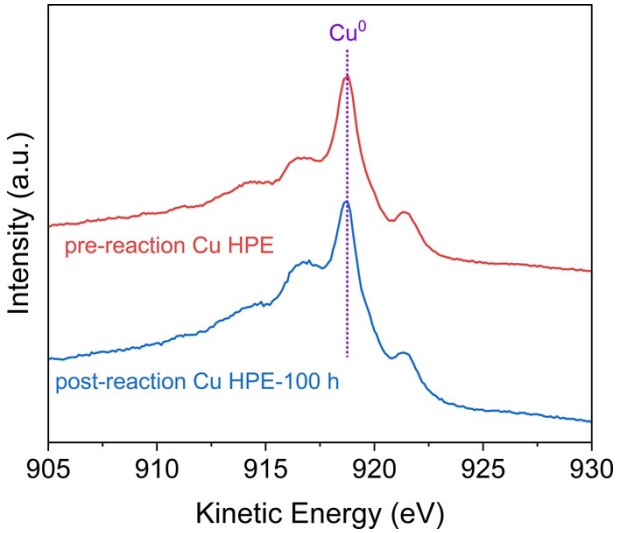

Fig. S4. Cu LMM Auger spectra of pre-reaction Cu HPE and post-reaction Cu HPE-100 h.

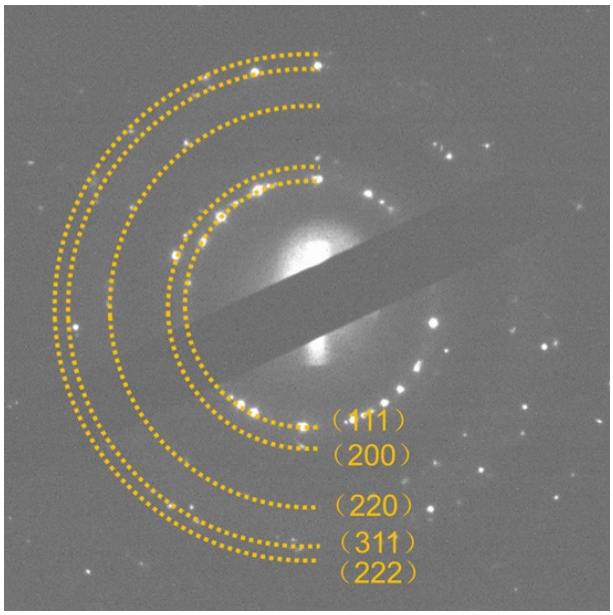

Fig. S5. SAED pattern of the Cu HPE.

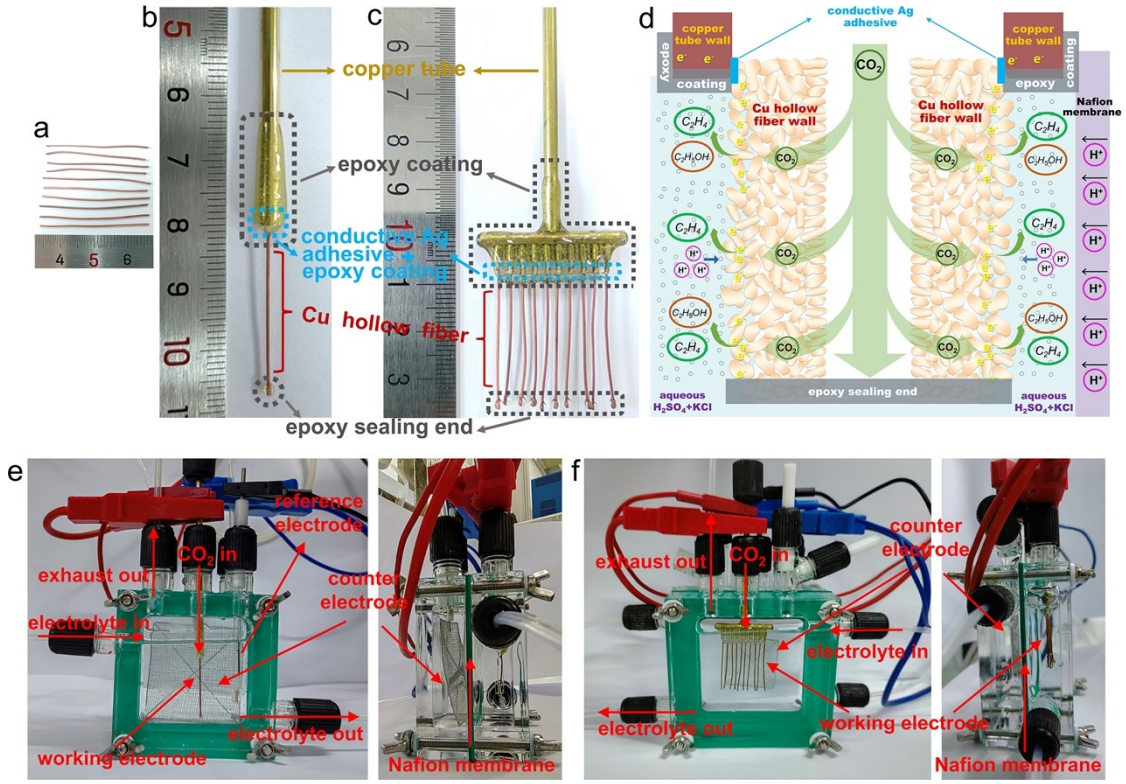

Fig. S6. Photographs of (a) self-supported Cu hollow fiber with single-component metallic copper, (b) single-tube Cu HPE, (c) 10-tube Cu HPE. (d) The schematic illustrations of single-tube Cu HPE showing the processes of CO_2 electroreduction. Side and cross-section views of the gas-tight H-cell with (e) single-tube Cu HPE and (f) 10-tube Cu HPE.

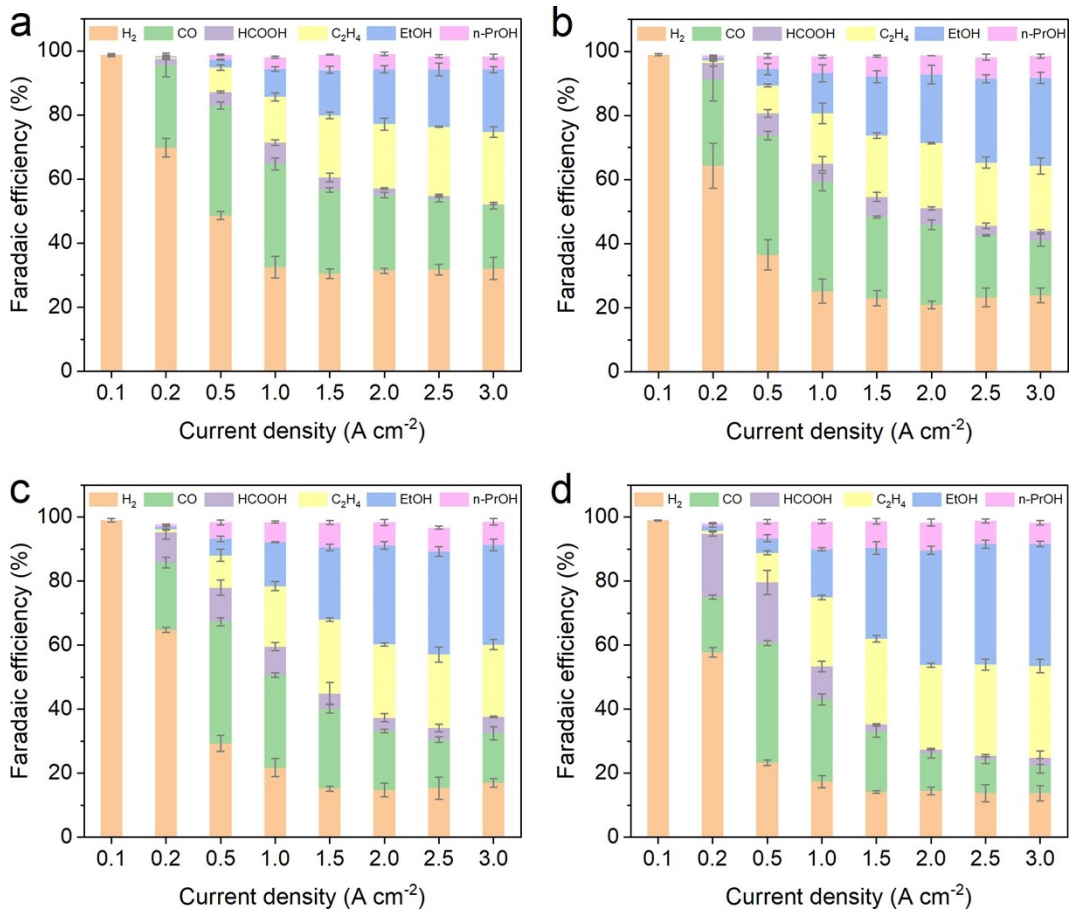

Fig. S7. Full product distributions of Cu HPE in pH=0.71 H_2SO_4 with (a) 0.5 M K^+, (b) 1.0 M K^+, (c) 2.0 M K^+, and (d) 3.0 M K^+.

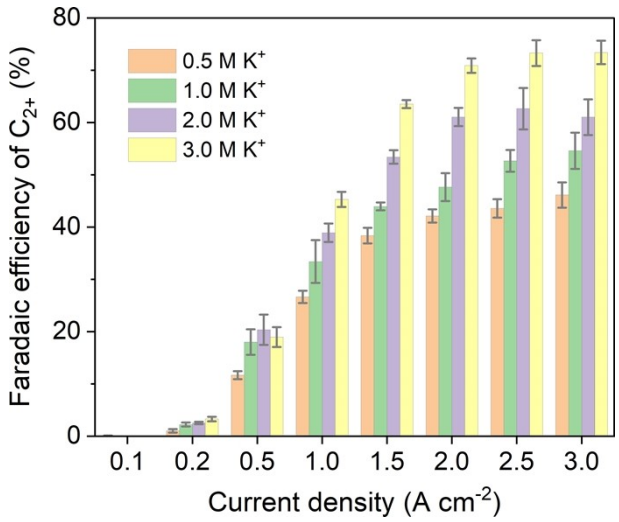

Fig. S8. The FE of C_{2+} s a function of current density over Cu HPE in pH=0.71 H_2SO_4 with different K^+ concentrations.

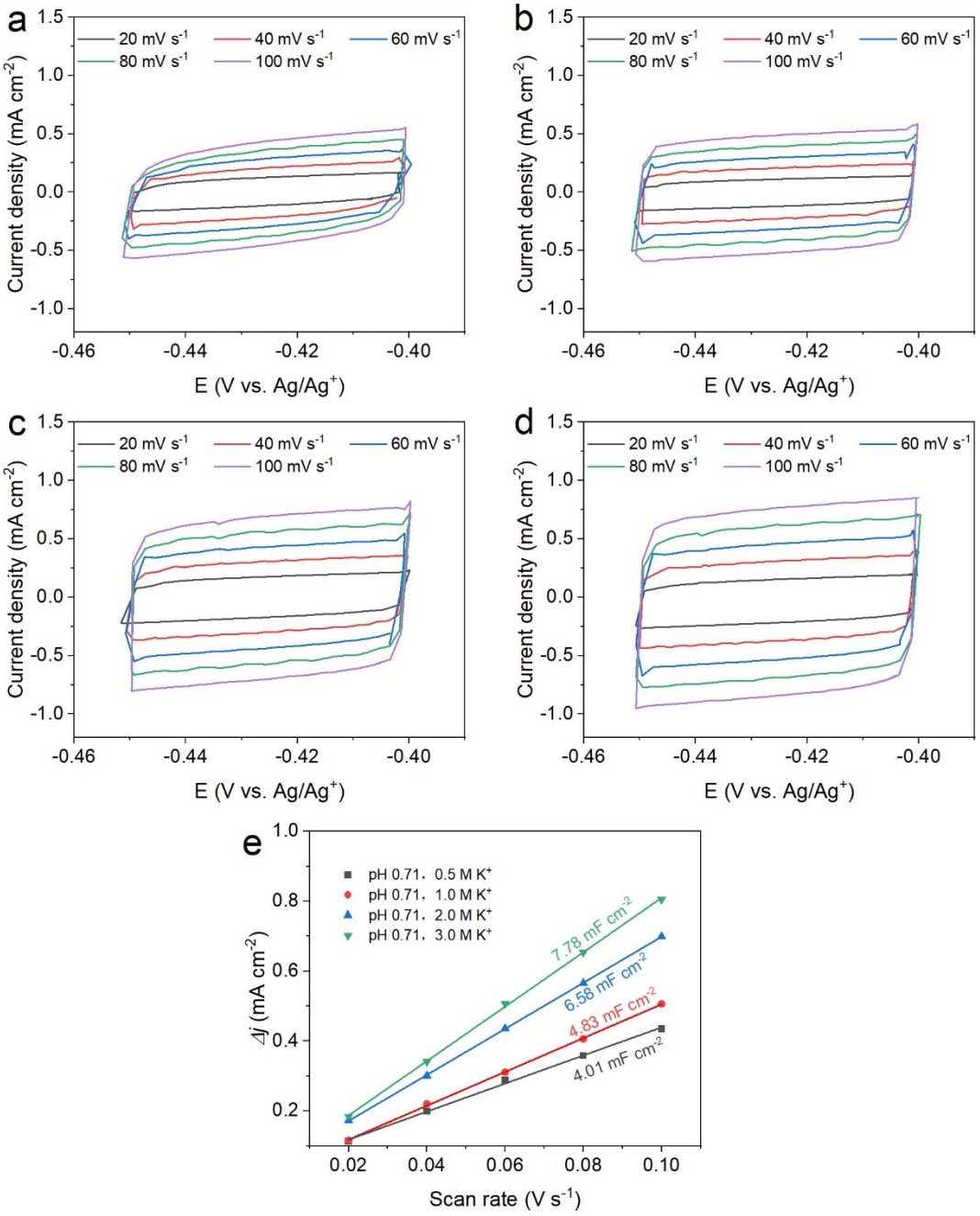

Fig. S9. Cyclic voltammetry curves of Cu HPE in pH=0.71 H_2SO_4 with (a) 0.5 M K^+, (b) 1.0 M K^+, (c) 2.0 M K^+, and (d) 3.0 M K^+. (e) The plot of current density against the scan rates.

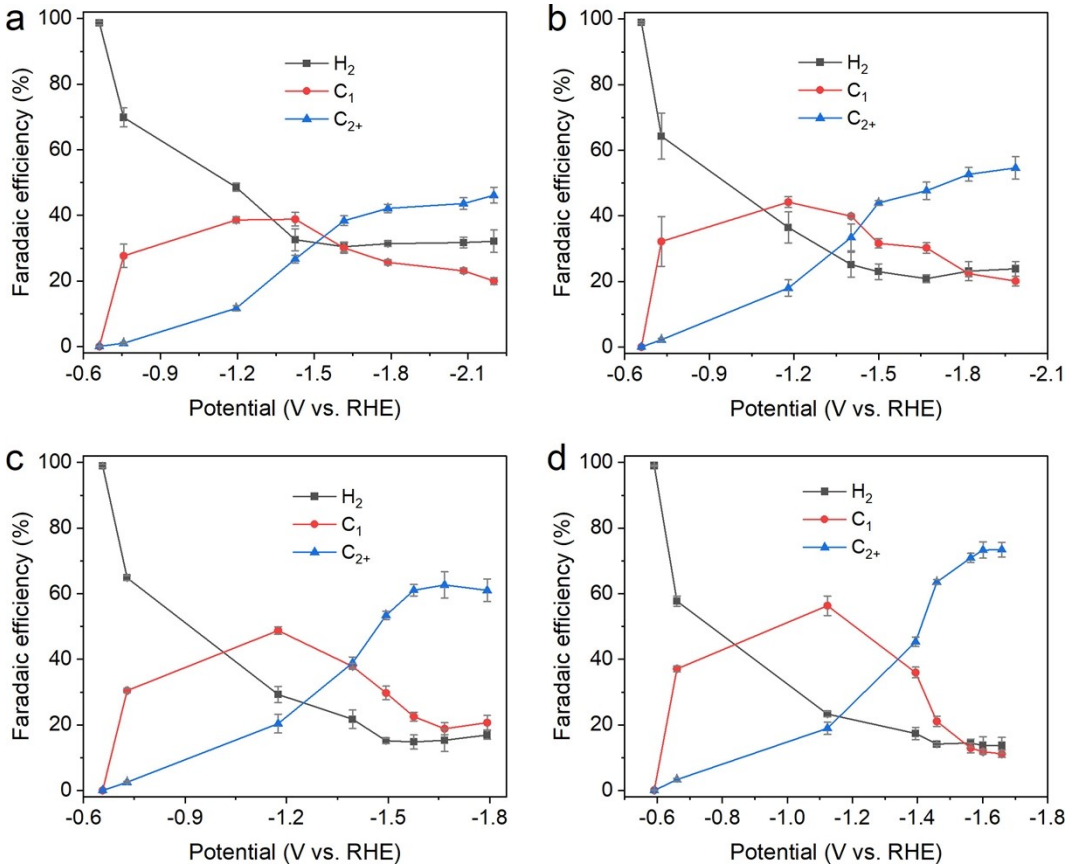

Fig. S10. FEs as a function of potential over Cu HPE in pH=0.71 H_2SO_4 with (a) 0.5 M K^+, (b) 1.0 M K^+, (c) 2.0 M K^+, and (d) 3.0 M K^+.

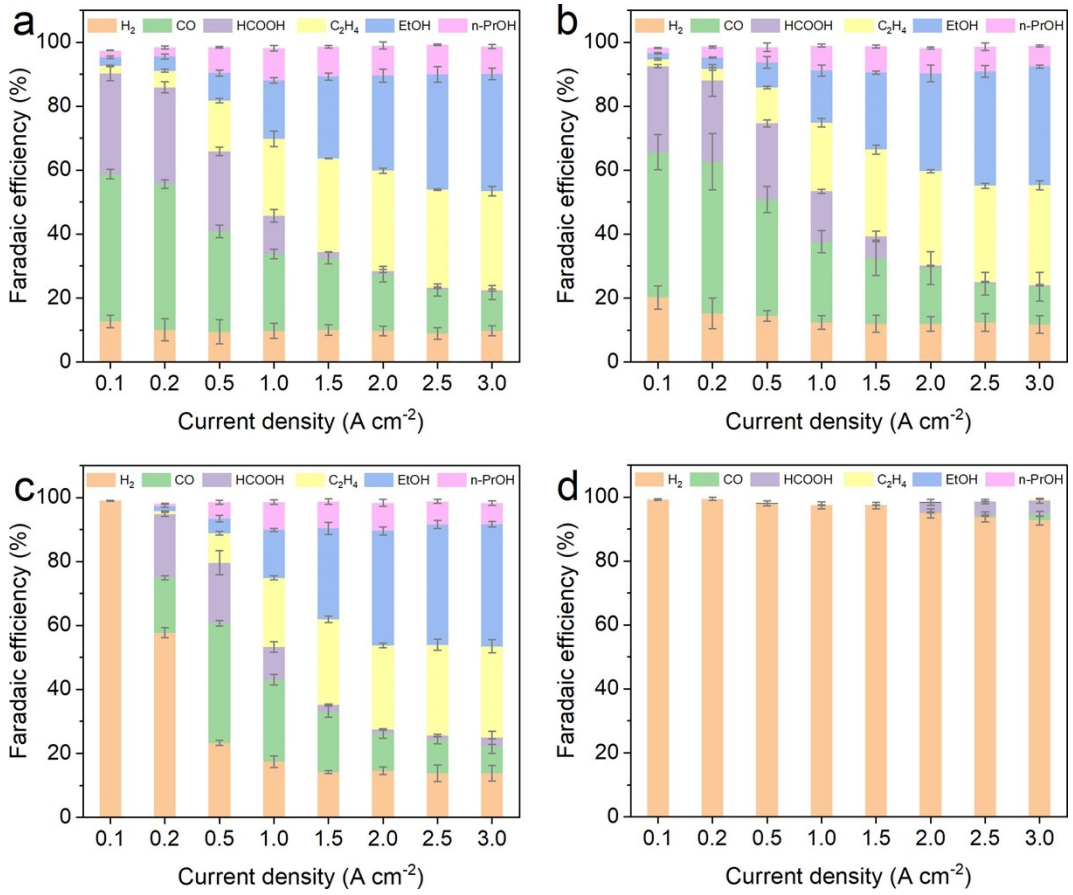

Fig. S11. Full product distributions of Cu HPE in H_2SO_4 with 3 M KCl at pH (a) 2.77, (b) 1.69, (c) 0.71, (d) 0.

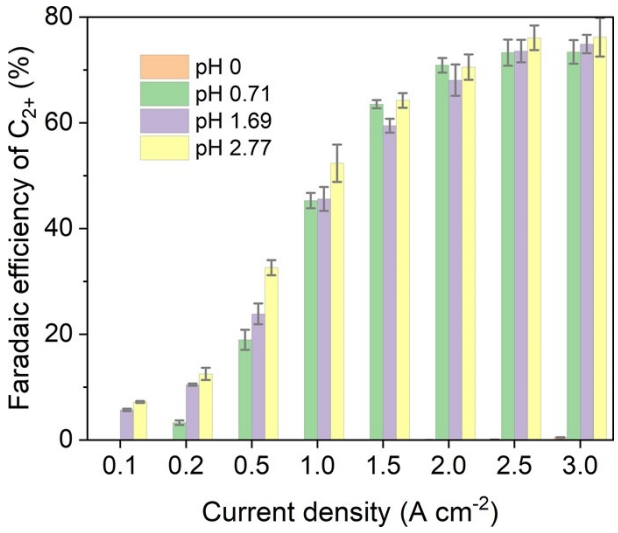

Fig. S12. The FE of C_{2+} as a function of current density over Cu HPE in H_2SO_4 with 3.0 M KCl at different pH.

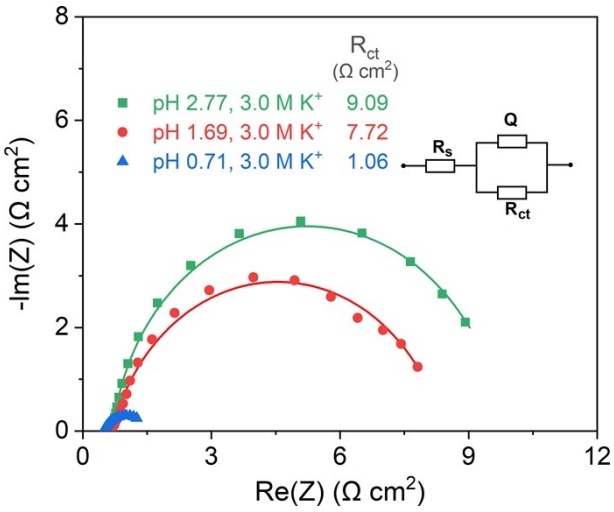

Fig. S13. EIS Nyquist plots of the Cu HPE. The inset shows the equivalent circuit.

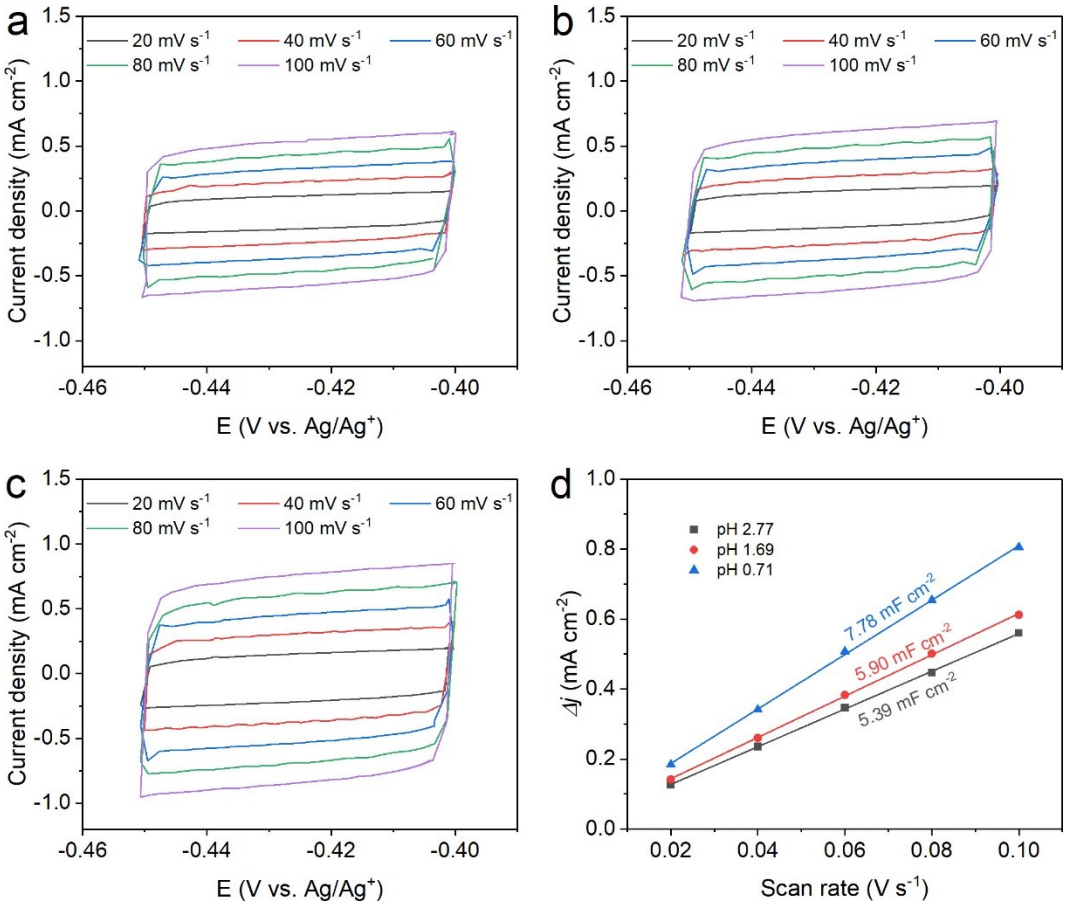

Fig. S14. Cyclic voltammetry curves of Cu HPE in H_2SO_4 with 3.0 M KCl at pH (a) 2.77, (b) 1.69, and (c) 0.71. (e) The plot of current density against the scan rates.

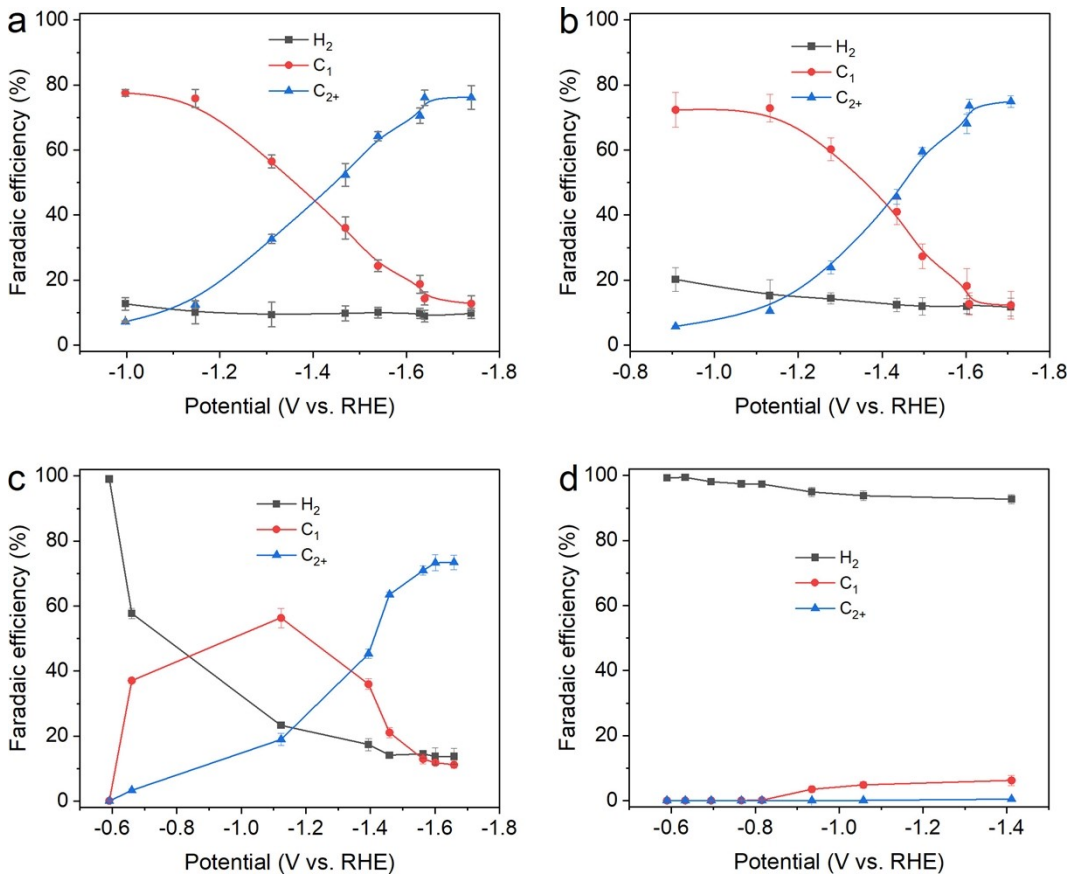

Fig. S15. FEs as a function of potential over Cu HPE in H_2SO_4 with 3.0 M KCl at pH (a) 2.77, (b) 1.69, (c) 0.71, and (d) 0.

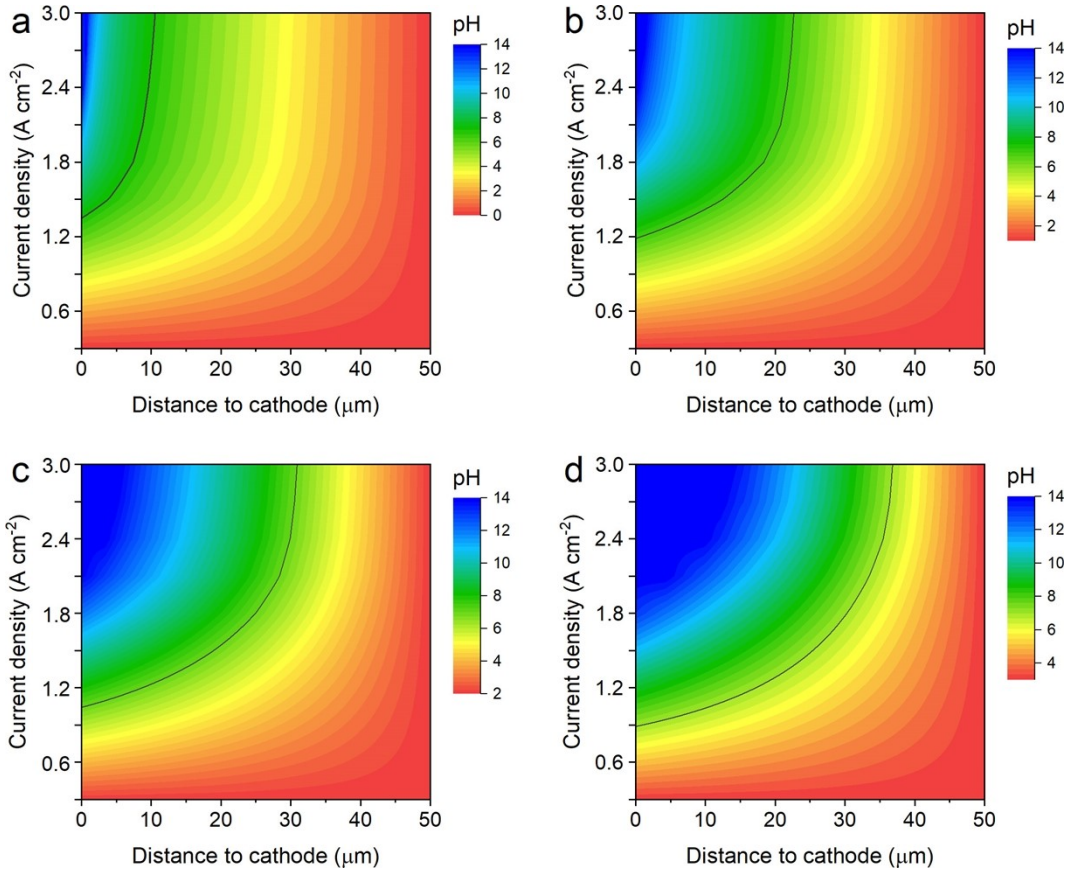

Fig. S16. Modeling of pH at different distances to cathode and current density in H_2SO_4 with 3 M KCl at pH (a) 0, (b) 1.0, (c) 2.0, (d) 3.0.

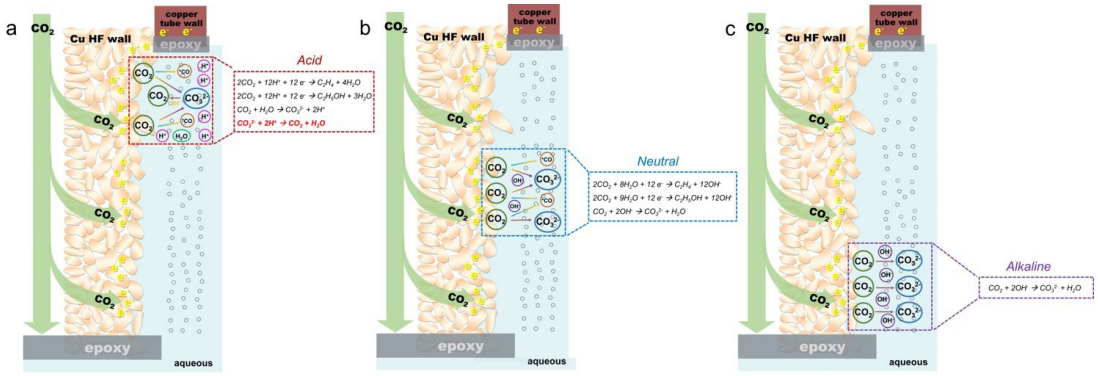

Fig. S17. Schematic illustrations of the reaction process involved in CO_2ERR over Cu HPE in in (a) acidic, (b) neutral, and (c) alkaline electrolytes respectively.

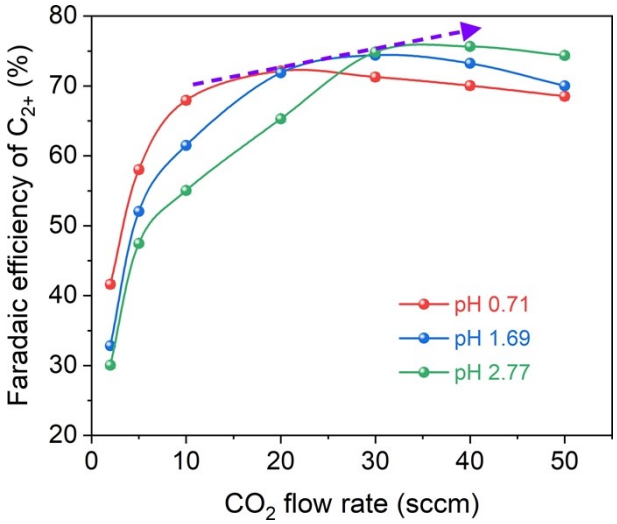

Fig. S18. FE of CO_2 to C_{2+} on Cu HPE at different CO_2 flow rates at constant current density of 3.0 A cm^{-2}.

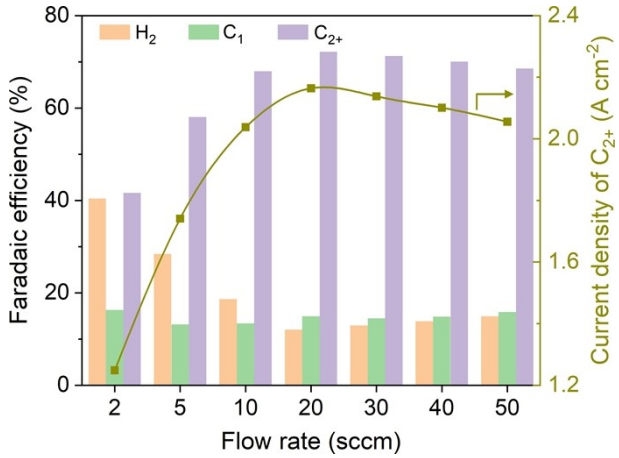

Fig. S19. FEs as a function of CO_2 flow rates in pH=0.71 H_2SO_4 solution with 3.0 M K^+ at 3.0 A cm^{-2}.

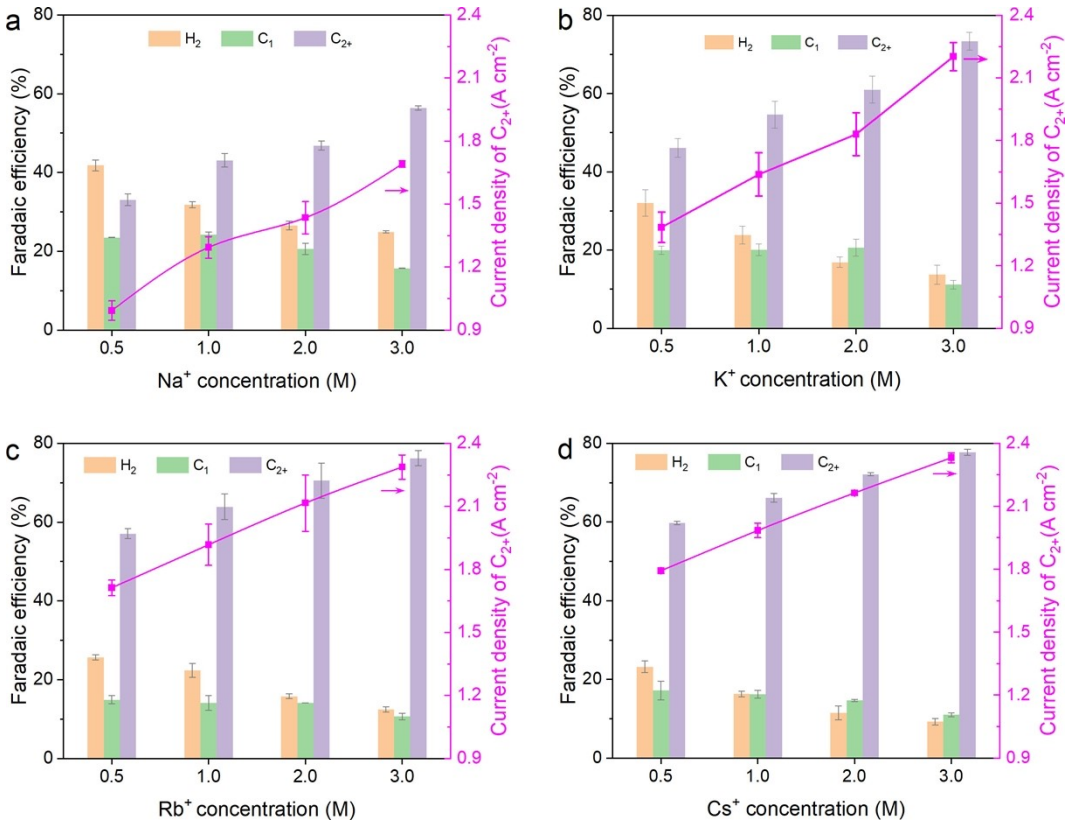

Fig. S20. (a) Na^+, (b) K^+, (c) Rb^+, (d) Cs^+ alkali metal ions concentration-dependent FE and partial current density of C_{2+}.

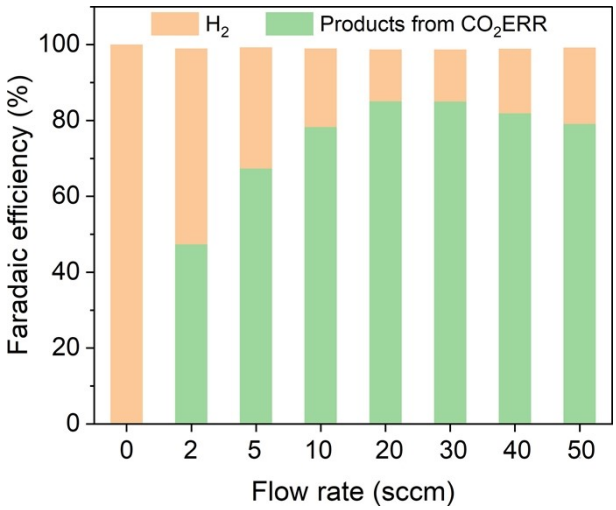

Fig. S21. FEs as a function of CO_2 flow rates over Cu HPE in pH=0.71 H_2SO_4 with 3.0 M KCl at constant current density of 3.0 A cm^{-2}.

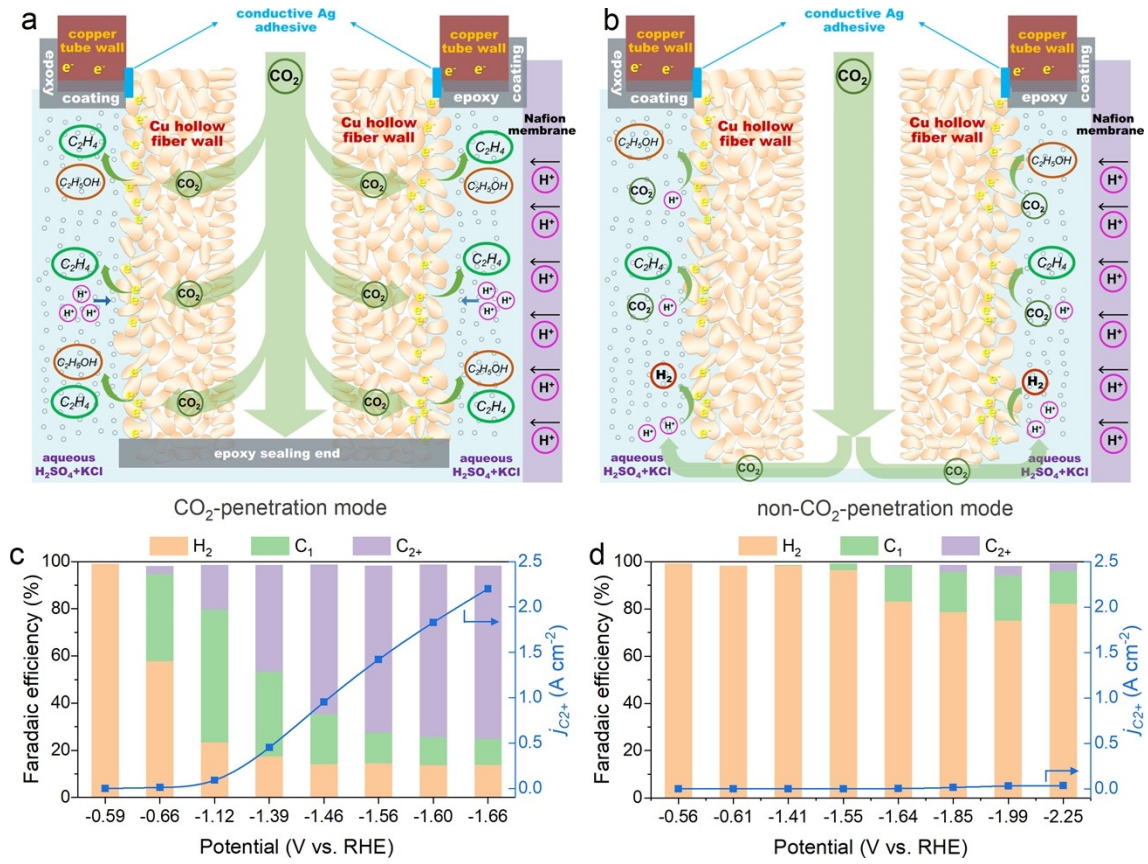

Fig. S22 Schematic illustrations and CO_2 electroreduction performance over Cu HPE with (a, c) the CO_2–penetration mode and (b, d) the non–CO_2–penetration mode, respectively.

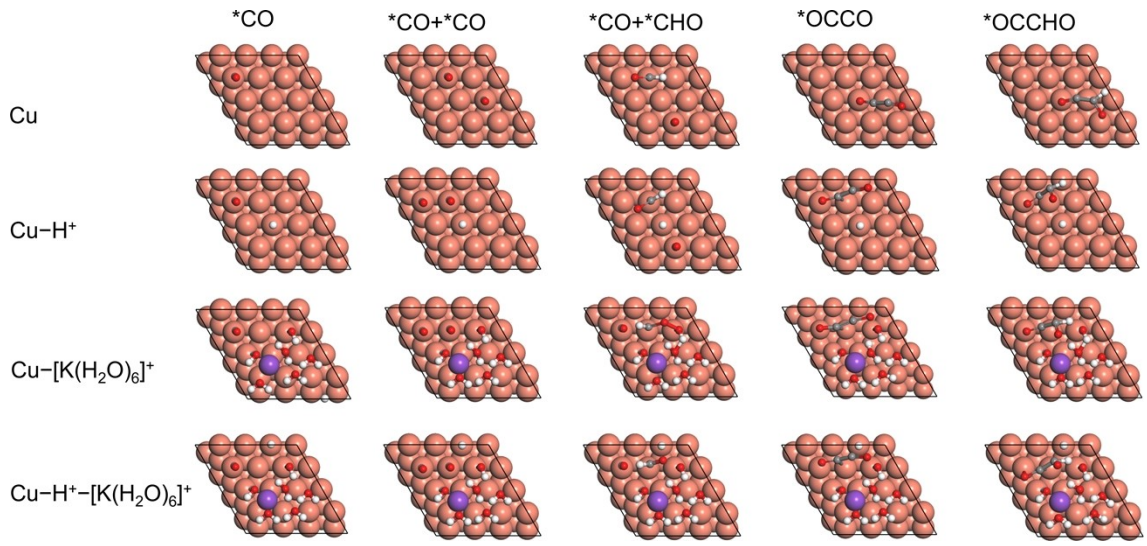

Fig. S23. Optimized surface slabs with adsorbed CO*, 2*CO, *CO+*CHO, *OCCO, and OCCHO* on Cu (11) slab, Cu (111) slab with H^+, Cu (111) slab with hydrated K^+ (Cu–$[K(H_2O)_6]^+$), and Cu (111) slab with H^+ and hydrated K^+ (Cu–H^+–$[K(H_2O)_6]^+$). The bronze, grey, red, white and purple balls represent Cu, C, O, H and K atoms, respectively.

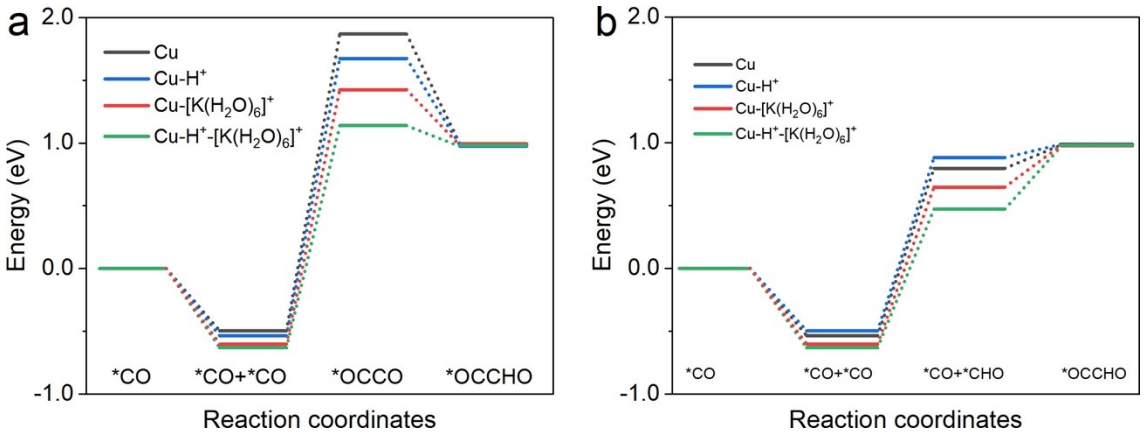

Fig. S24. Free energy of the C−C reaction pathway: (a) *CO dimerization and (b) *CO+*CHO coupling.

Table S1. Temperature recording of cathode solution during CO_2 electrolysis.

Reaction time (min)	Catholyte temperature without pump circulation (℃)	Catholyte temperature with pump circulation (℃)
0	25.0	25.0
5	26.1	25.5
10	27.5	26.1
30	29.6	26.5
60	31.8	26.4
90	33.2	26.6
120	36.4	26.5

Table S2. The H^+ concentration of the catholyte solution in the electrolysis of 1 h at 2 A cm^{-2} was recorded by acid-base titrations.

Reaction time (min)	H^+ concentration (mol L^{-1})
0	0.191
15	0.186
30	0.191
45	0.187
60	0.190

Table S3. The amount of dissolved Cu in the outlet electrolyte quantified by ICP-OES.

Reaction time	Dissolved Cu
30 min (OCP)	Not detected
1.0 h (stability test)	Not detected
5.0 h (stability test)	Not detected
10 h (stability test)	Not detected
20 h (stability test)	Not detected
50 h (stability test)	Not detected

Table S4. Performance comparison with previously reported acidic CO_2ERR systems. Only C_{2+} producing in acidic systems were compared.

Catalyst	Stability (h)	EE_{C2+} (%)	SPCE (%)	FE_{C2+} (%)	J_{total} (A cm^{-2})	Ref.
Cu HPE	100	29	52	73	3.0	This work
PCRL-Cu	8	13	40	40	0.1	[5]
COF:PFSA-Cu	30	25	25	75	0.2	[6]
Cu/C	4	~11	/	45	0.54	[7]
ER-CuNS	30	~30	34	84	0.67	[8]
Cu/PFSA	12	12	47	50	1.2	[9]

Table S5. Performance comparison with previously reported alkaline and neutral CO_2ERR systems. Only C_{2+} producing in alkaline or neutral systems were compared.

Catalyst	Electrolyte	Stability (h)	FE_{C2+} (%)	j_{C2+} (A cm^{-2})	Ref.
Cu HPE	0.05 M H_2SO_4+3.0 M KCl	100	73	2.20	This work
Cu-nr/CC3	1.0 M KOH	10	76.1	1.29	[10]
F-Cu	0.75 M KOH	40	80	1.28	[11]
3D-CIBH	7.0 M KOH	60	78.2	1.21	[12]
N-Cu	1.0 M KOH	6	73.7	0.91	[13]
Cu interface	3.5 M KOH+5.0 M KI	150	80	0.6	[14]
CuONPs	1.0 M KCl	3	73	1.74	[15]
AC-Cu HF	3.5 M KCl	168	64.8	1.29	[16]
ED-Cu	2.0 M KCl	30	67	0.13	[17]
OD-Cu	1.0 M $KHCO_3$	10	68	0.34	[18]
Cu-12	0.5 M $KHCO_3$	180	86	0.28	[19]

Table S6. Comparison of acidic electrochemical CO_2 reduction at a flow rate of ~2 sccm with other recent reports. Only C_{2+} producing in acidic systems were compared.

Catalyst	Flow rate (sccm)	FE_{H2} (%)	j_{C2+} (A cm^{-2})	$SPCE_{C2+}$ (%)	Ref.
Cu HPE	2	40	1.25	52	*This Work*
Cu /PFSA	3	~45	~0.54	~47	*9*
ER-CuNS	2	<38	~0.49	54	*8*
CG-medium Cu	1	~33	~0.08	~9	*20*
PCRL-Cu	2	~30	~0.05	~40	*5*

Table S7. Comparison of *wt%* of ethanol after 12h reaction with other recent reports.

Catalyst	*Electrolyte*	*FE (%)*	j_{total} *(A cm^{-2})*	j_{EtOH} *(A cm^{-2})*	*wt (%)*	*Ref.*
Cu HPE	0.05 M H_2SO_4+3.0 M KCl	38	3.0	1.14	0.88**	*This Work*
Cu/PFSA	1 M H_3PO_4+3 M KCl	11	1.2	0.13	0.51*	*9*
ER-CuNS	0.05 M H_2SO_4+3.0 M KCl	22	0.7	0.15	0.31*	*8*
COF:PFSA-Cu	H_3PO_4(3 M KCl, pH 1.0)	14	0.4	0.06	0.23*	*6*
Cu-nr/CC3	1 M KOH	24	1.7	0.41	1.57*	*10*
F-Cu	0.75 M KOH	16	1.2	0.19	0.74*	*11*
AEI-OD-Cu	1 M KOH	26	0.6	0.16	0.60*	*21*
TWN-$Cu_{13.35}$-600-SACs	0.5 M $CsHCO_3$	82	0.05	0.037	0.14*	*22*

**: The result based on the off-line GC measurement.

*: The results were calculated based on the assumed catholyte volume (35 mL).

Table S8. pH values of different cathode electrolytes.

Electrolyte	pH
0.5 M H_2SO_4+3.0 M KCl	0.00
0.05 M H_2SO_4+3.0 M KCl	0.71
0.005 M H_2SO_4+3.0 M KCl	1.69
0.0005 M H_2SO_4+3.0 M KCl	2.77

Table S9. Solution resistances of sulfuric acid solution with 3.0 M KCl at various pH values.

pH	Charge transfer resistance (Ohm cm^2)	Solution resistance (Ohm cm^2)
0.71	1.06	0.50
1.69	7.72	0.66
2.77	9.09	0.72

Table S10. Diffusion coefficient for different species.[9]

Species	D [10^{-9} m^2 s^{-1}]
H^+	9.311
OH^-	5.293
HCO_3^-	1.185
CO_3^{2-}	0.923
CO_2	1.910

References

1 C. Zhu, G. Shen, W. Chen, X. Dong, G. Li, Y. Song, W. Wei, Y. Sun, *J. Power Sources*, 2021, **495**, 229814.

2 G. Kresse, D. Joubert, *Phys. Rev. B*, 1999, **59**, 1758-1775.

3 J. P. Perdew, K. Burke, M. Ernzerhof, *Phys. Rev. Lett.*, 1996, **77**, 3865-3868.

4 K. Momma, F. Izumi, *J. Appl. Crystallogr.*, 2011, **44**, 1272-1276.

5 C. P. O'Brien, R. K. Miao, S. Liu, Y. Xu, G. Lee, A. Robb, J. E. Huang, K. Xie, K. Bertens, C. M. Gabardo, J. P. Edwards, C.-T. Dinh, E. H. Sargent, D. Sinton, *ACS Energy Lett.*, 2021, **6**, 2952-2959.

6 Y. Zhao, L. Hao, A. Ozden, S. Liu, R. K. Miao, P. Ou, T. Alkayyali, S. Zhang, J. Ning, Y. Liang, Y. Xu, M. Fan, Y. Chen, J. E. Huang, K. Xie, J. Zhang, C. P. O'Brien, F. Li, E. H. Sargent, D. Sinton, *Nat. Synth.*, **2**, 403-412.

7 J. Gu, S. Liu, W. Ni, W. Ren, S. Haussener, X. Hu, *Nat. Catal.*, 2022, 5, 268-276.

8 Z. Ma, Z. Yang, W. Lai, Q. Wang, Y. Qiao, H. Tao, C. Lian, M. Liu, C. Ma, A. Pan, H. Huang, *Nat. Commun.*, 2022, **13**, 7596.

9 J. E. Huang, F. Li, A. Ozden, A. S. Rasouli, F. P. G. de Arquer, S. Liu, S. Zhang, M. Luo, X. Wang, Y. Lum, Y. Xu, K. Bertens, R. K. Miao, C.-T. Dinh, D. Sinton, E. H. Sargent, *Science*, 2021, **372**, 1074-1078.

10 C. Chen, X. Yan, Y. Wu, S. Liu, X. Zhang, X. Sun, Q. Zhu, H. Wu, B. Han, *Angew. Chem. Int. Ed.*, 2022, **61**, e202202607.

11 W. Ma, S. Xie, T. Liu, Q. Fan, J. Ye, F. Sun, Z. Jiang, Q. Zhang, J. Cheng, Y. Wang, *Nat. Catal.*, 2020, **3**, 478-487.

12 F. P. Garcia de Arquer, C. T. Dinh, A. Ozden, J. Wicks, C. McCallum, A. R. Kirmani, D. H. Nam, C. Gabardo, A. Seifitokaldani, X. Wang, Y. C. Li, F. Li, J. Edwards, L. J. Richter, S. J. Thorpe, D. Sinton, E. H. Sargent, *Science*, 2020, **367**, 661-666.

13 M. Zheng, P. Wang, X. Zhi, K. Yang, Y. Jiao, J. Duan, Y. Zheng, S. Z. Qiao, *J. Am. Chem. Soc.*, 2022, **144**, 14936-14944.

14 C.-T. Dinh, T. Burdyny, M. G. Kibria, A. Seifitokaldani, C. M. Gabardo, F. P. G. de Arquer, A. Kiani, J. P. Edwards, P. De Luna, O. S. Bushuyev, C. Zou, R. Quintero-Bermudez, Y. Pang, D. Sinton, E. H. Sargent, *Science*, 2018, **360**, 783-787.

15 A. Inoue, T. Harada, S. Nakanishi, K. Kamiya, *EES Catal.*, 2023, **1**, 9-16.

16 C. Zhu, Y. Song, X. Dong, G. Li, A. Chen, W. Chen, G. Wu, S. Li, W. Wei, Y. Sun, *Energy Environ. Sci.*, 2022, **15**, 5391-5404.

17 X. Zhang, J. Li, Y. Y. Li, Y. Jung, Y. Kuang, G. Zhu, Y. Liang, H. Dai, *J. Am. Chem. Soc.*, 2021, **143**, 3245-3255.

18 Y. C. Tan, K. B. Lee, H. Song, J. Oh, *Joule*, 2020, **4**, 1104-1120.

19 F. Li, A. Thevenon, A. Rosas-Hernandez, Z. Wang, Y. Li, C. M. Gabardo, A. Ozden, C. T. Dinh, J. Li, Y. Wang, J. P. Edwards, Y. Xu, C. McCallum, L. Tao, Z. Q. Liang, M. Luo, X. Wang, H. Li, C. P. O'Brien, C. S. Tan, D. H. Nam, R. Quintero-Bermudez, T. T. Zhuang, Y. C. Li, Z. Han, R. D. Britt, D. Sinton, T. Agapie, J. C. Peters, E. H. Sargent, *Nature*, 2020, **577**, 509-513.

20 M. Fan, J. E. Huang, R. K. Miao, Y. Mao, P. Ou, F. Li, X.-Y. Li, Y. Cao, Z. Zhang, J. Zhang, Y. Yan, A. Ozden, W. Ni, Y. Wang, Y. Zhao, Z. Chen, B. Khatir, C. P. O'Brien, Y. Xu, Y. C. Xiao, G. I. N. Waterhouse, K. Golovin, Z. Wang, E. H. Sargent and D. Sinton, *Nat. Catal.*, 2023, DOI: 10.1038/s41929-023-01003-5.

21 Y. Zhao, X. Zu, R. Chen, X. Li, Y. Jiang, Z. Wang, S. Wang, Y. Wu, Y. Sun and Y. Xie, *J. Am. Chem. Soc.*, 2022, **144**, 10446-10454.

22 W. Xia, Y. Xie, S. Jia, S. Han, R. Qi, T. Chen, X. Xing, T. Yao, D. Zhou, X. Dong, J. Zhai, J. Li, J. He, D. Jiang, Y. Yamauchi, M. He, H. Wu and B. Han, *J. Am. Chem. Soc.*, 2023, **145**, 17253-17264.